Strain-tunable photovoltaic efficiency and symmetry-breaking enhanced photocurrent in Janus WSTe/BP heterostructures

You Xie (解忧) [a, b *], Jiaqi Li (李家琪) [a], Xiaosa Xiao (肖潇飒) [a], Limei Hao (郝丽梅) [a], Tao Zhang (张涛) [a]

[a] *College of Sciences, Xi'an University of Science and Technology, Xi'an 710054, China*

[b] *College of Chemistry and Chemical Engineering, Xi'an University of Science and Technology, Xi'an 710054, China*

Abstract: Janus transition-metal dichalcogenides (TMDs) break the inversion symmetry of conventional TMDs and introduce an out-of-plane dipole moment and built-in electric field, which effectively tailor electronic structures and carrier transport features for high-performance optoelectronic devices. Using first-principles calculations, we investigate two stacking configurations of Janus WSTe and boron phosphide (WSTe/BP) van der Waals heterostructures under biaxial strain ranging from −8% to +8%. Both stacking configurations exhibit robust dynamical and thermodynamic stability as well as typical type-II band alignment, with bandgaps of 1.23 eV (TeWS/BP) and 0.67 eV (SWTe/BP). The weaker interfacial dipole in TeWS/BP enables strain-driven band-alignment transitions, while SWTe/BP preserves type-II behavior due to strong interlayer electronic coupling. TeWS/BP delivers a maximum power conversion efficiency (PCE) of 20.98% under +2% tensile strain, far outperforming the 5.26% PCE of SWTe/BP. Combined with nonequilibrium Green's function simulations, the photogalvanic effect reveals that asymmetric contacts drastically boost the armchair-direction photocurrent of TeWS/BP to 18.0 a_0^2/photon, about 360 times that of symmetric contacts, with a maximum polarization extinction ratio reaching 327.2.

* Corresponding author.

E-mail address: xieyou@xust.edu.cn (Y. Xie).

These results clarify stacking and electrode effects on device performance and highlight Janus WSTe/BP as a promising platform for next-generation photovoltaics and photodetectors.

Keywords: van der Waals heterostructures, Power conversion efficiency, Photovoltaic effect, Biaxial strain, First-principles calculations

PACS: 79.60.Jv, 84.60.Jt, 72.40.+w, 77.80.bn, 63.20.dk

1. Introduction

The rapid advancement of nanotechnology and quantum materials has positioned two-dimensional (2D) materials at the forefront of condensed matter physics and materials science, owing to their unique physical properties and substantial potential for next-generation optoelectronic devices. Since graphene was discovered, the 2D material family has expanded to include transition metal dichalcogenides (TMDs), hexagonal boron nitride, phosphorene, and other systems, exhibiting a rich variety of electronic, optical, and mechanical characteristics. Among them, TMDs stand out as particularly promising candidates for future optoelectronic applications because of their tunable direct bandgaps, strong light–matter interactions, and layer-dependent electronic properties [1–8].

In 2017, the experimental synthesis of Janus TMDs (such as MoSSe and WSSe) realized an intrinsic out-of-plane dipole moment by breaking the in-plane inversion symmetry of traditional TMDs, providing a new strategy for band engineering and photoexcited carrier separation [9–12]. Janus WSTe monolayers have attracted wide attention due to their moderate direct bandgap, good stability, and high optical absorption. Their electronic properties can be effectively tuned by external fields, which helps form type-II band alignment for efficient charge separation [13]. Recent investigations have shown that Janus

MoSeTe/WSeTe van der Waals heterostructure (vdWH) achieve type-II band alignment through Ge–Se interfacial interactions, with predicted power conversion efficiencies (PCE) of approximately 20% [14]. Similarly, the $TeGa_2Se$/InS heterostructure exhibits a peak PCE of 23.2% under 4% biaxial compressive strain, highlighting the substantial photovoltaic potential of Janus systems [13]. Notably, the WSTe monolayer features a tunable bandgap, carrier mobilities on the order of 10^4 $cm^2 \cdot V^{-1} \cdot s^{-1}$, and an optical absorption coefficient reaching up to 10^5 cm^{-1} in the visible region [15].

As a typical 2D semiconductor, boron phosphide (BP) has a tunable direct bandgap (0.8–1.8 eV), ultrahigh carrier mobility (~10^6 $cm^2 \cdot V^{-1} \cdot s^{-1}$), and excellent strain tolerance [16–20], making it an ideal partner for constructing WSTe-based heterostructures. Recent studies have shown that vdWHs combining BP and 2D polar materials exhibit optimized optoelectronic performance. For example, the BP/Sc_2CF_2 heterostructure undergoes a transition from semiconducting to gapless semiconducting behavior under an external electric field, offering rich possibilities for band engineering [21–23]. Janus MoSTe/BP devices achieve an ultrahigh extinction ratio (228.6) under asymmetric contacts [24], and BC_6N/Janus MoSSe structures generate a large photocurrent (61.55 a_0^2/photon) along the armchair direction [25]. Experimentally, the formation of a WSe_2/$CsPbI_3$ has been shown to boost the photocurrent from 2.38 na to 38.5 na [26]. These results inspire us to design Janus WSTe/BP heterostructures and explore their strain-tunable optoelectronic properties and photogalvanic effect.

In this work, we use first-principles calculations to study the electronic structures, optical properties, and photovoltaic performance of Janus WSTe/BP vdWHs under biaxial strain (–8%

to +8%). We also use non-equilibrium Green's function (NEGF) simulations to analyze the photogalvanic effect (PGE) under different electrode configurations, revealing their application potential in high-efficiency photovoltaics and polarization-sensitive photodetectors.

2. **Computational methods and details**

The electronic properties of Janus WSTe/BP heterostructures were investigated using first-principles density functional theory (DFT) calculations with the Vienna Ab initio Simulation Package (VASP) [27–29]. Electronic exchange-correlation interactions were treated using the Perdew-Burke-Ernzerhof (PBE) functional, with electronic structure and optical absorption properties further refined using the Heyd-Scuseria-Ernzerhof (HSE06) hybrid functional [30,31]. Van der Waals interactions were accounted for through the DFT-D3 correction method [29,32]. A vacuum layer of 20 Å was applied along the out-of-plane direction to eliminate spurious interlayer interactions. Structural relaxations and property calculations were performed using a 7 × 7 × 1 Monkhorst–Pack k-point mesh and a plane-wave cutoff energy of 450 eV [33]. Convergence criteria for structural optimization were set to 10^{-3} eV/Å for atomic forces and 10^{-6} eV for total energy changes.

Phonon dispersion calculations were performed using density functional perturbation theory with a 7 × 7 × 1 Monkhorst–Pack k-point mesh and a plane-wave cutoff energy of 450 eV. Convergence thresholds were set to 10^{-3} eV/Å for atomic forces and 10^{-8} eV for the total energy. Ab initio molecular dynamics (AIMD) simulations were conducted at a constant temperature of 300 K, employing a total of 10,000 molecular dynamics steps (NSW = 10,000). This setup yielded an overall simulation duration of 10 ps, corresponding to a time step of

POTIM=1 fs.

Optical properties were calculated from the frequency-dependent dielectric tensor under the independent particle approximation. The PCE was assessed via the modified Shockley–Queisser equation, which accounts for built-in electric field effects: $\eta = \frac{\beta_{FF} V_{OC} J_{SC}}{P_{solar}} = \frac{0.65(E_{gd} - \Delta E_c - 0.3) \int_{E_{gd}}^{\infty} \frac{P(\hbar\omega)}{\hbar\omega} d(\hbar\omega)}{\int_0^{\infty} P(\hbar\omega) d(\hbar\omega)}$. Here, $\beta_{FF} = 0.65$ is adopted as a representative fill factor for 2D vdWH solar cells, and the open-circuit voltage is defined as $V_{OC} = E_{gd} - \Delta E_c - 0.3$. In this expression, E_{gd} refers to the bandgap of the donor material, ΔE_c denotes the conduction band offset, and the constant term of 0.3 eV compensates for non-ideal interfacial effects.

Photodetectors based on Janus WSTe/BP were modeled, and photocurrents were computed using the NanoDcal code, which integrates DFT with the NEGF method [34]. According to the theoretical expression adopted in this work:

$$J_L^{(ph)} = \frac{ie}{h} \int \Big\{ \cos^2\theta Tr\left\{\Gamma_{\mathrm{L}}\left[G_1^{<(ph)} + f_{\mathrm{L}}\left(G_1^{>(ph)} - G_1^{<(ph)}\right)\right]\right\} + \sin^2\theta\, Tr\left\{\Gamma_{\mathrm{L}}\left[G_2^{<(ph)} + f_{\mathrm{L}}\left(G_2^{>(ph)} - G_2^{<(ph)}\right)\right]\right\} + 2\sin(2\theta)\, Tr\left\{\Gamma_{\mathrm{L}}\left[G_3^{<(ph)} + f_{\mathrm{L}}\left(G_3^{>(ph)} - G_3^{<(ph)}\right)\right]\right\}\Big\} \mathrm{d}E$$

Where $G_{1,2,3}^{>/<(\mathrm{ph})}$ denotes electron-photon-interaction Green's functions dependent on photon frequency ω; f_{L} is the Fermi-Dirac distribution function; Γ_{L} represents electrode self-energy. The prefactor reads $C_0 = \frac{e^2\hbar\sqrt{\mu_r \epsilon_r}}{2Nm^2\omega\epsilon c} I_\omega$. Normalized photocurrent is defined as $I_{\mathrm{ph}} = \frac{J_L^{(ph)}}{eI_\omega}$, where I_ω is incident photon flux, m represents the electron mass and e stands for the elementary charge. The formalism for calculating photocurrents under linearly polarized light has been documented in earlier work [35–37]. Considering different crystallographic

orientations, we employ 1 × 11 × 1 k-points for the zigzag direction and 11 × 1 × 1 k-points for the armchair direction. All device transport simulations adopt the GGA-PBE96 functional to reach static self-consistency under zero external bias voltage.

3. **Results and discussion**

3.1 Structure and stability of Janus WSTe/BP vdWHs

After full structural relaxation, the lattice constants of monolayer BP and Janus WSTe are determined to be 3.215 Å and 3.359 Å, respectively, as shown in Fig 1(a) and (b). These structural parameters are consistent with previous reports [38–40]. To determine the optimal stacking mode of the heterostructure, we constructed multiple configurations and selected the two most stable ones by comparing their binding energies. The two stacking configurations, TeWS/BP and SWTe/BP, have interlayer distances d of 3.413 Å and 3.736 Å, respectively (Fig 1(c) and (d)). These values directly reflect the strength of van der Waals interactions. The two stacking modes correspond to distinct interlayer atomic registries, which strongly influence orbital hybridization and interfacial electronic coupling. The difference arises from the varying interaction strengths of the constituent atoms with the BP surface: Te atoms, owing to their larger atomic radius and different electronegativity, form stronger van der Waals interactions with BP, resulting in a smaller interlayer spacing. By controlling the relative orientation and stacking geometry, distinct interfacial coupling strengths and electronic structures can be achieved while preserving the same chemical composition. The subsequent optoelectronic calculations are based on these optimized geometries.

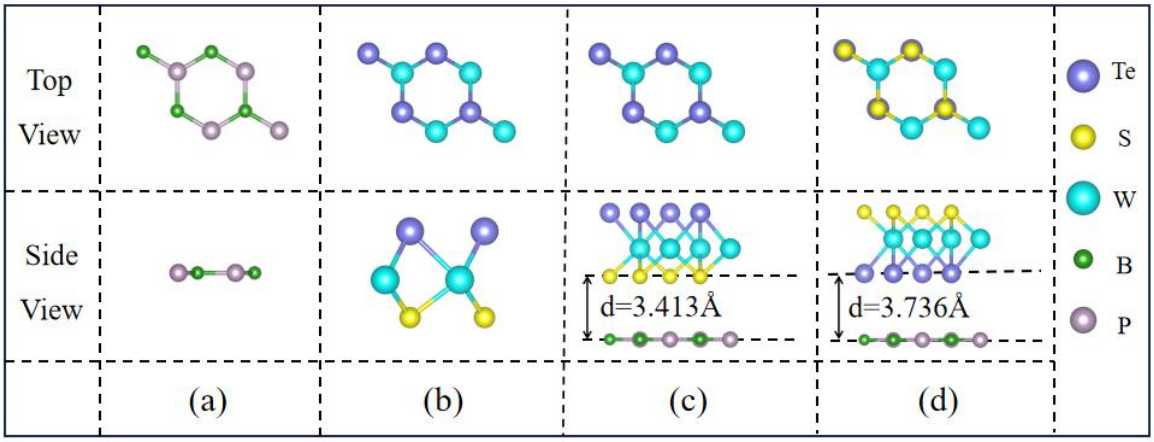


Fig. 1. Structural models: (a) 2 × 2 × 1 BP, (b) 2 × 2 × 1 Janus WSTe, (c) TeWS/BP, and (d) SWTe/BP.

Figs. 2(a) and (c) present the phonon dispersion of the TeWS/BP and SWTe/BP vdWHs, respectively. All acoustic branches lie above zero frequency, with no imaginary frequencies observed, confirming the dynamical stability of both heterostructures. Figs. 2(b) and (d) show the results of AIMD simulations over a 10 ps trajectory to probe thermal fluctuation behavior. To quantitatively evaluate the energy fluctuations, we calculated the average energy fluctuation per atom in the AIMD simulations for SWTe/BP and TeWS/BP, which are about 0.0035 eV/atom and 0.0016 eV/atom, respectively. These values all meet the threshold requirements of the AIMD stability criterion, fully confirming that both heterostructures possess good thermodynamic stability at room temperature. The temperature curves remain stable around 300 K, with fluctuations consistent with the expected statistical behavior of the NVT ensemble. After 10 ps of simulation, both vdWHs retain their intact layered morphologies, with no signs of interlayer separation, atomic diffusion, or structural reconstruction. This indicates that the van der Waals interfaces maintain stable binding under finite temperatures, and the interlayer interactions in both heterostructures are sufficiently strong to resist thermal agitation. These results demonstrate adequate stability under ambient

conditions, supporting the potential application of these heterostructures in optoelectronic devices.

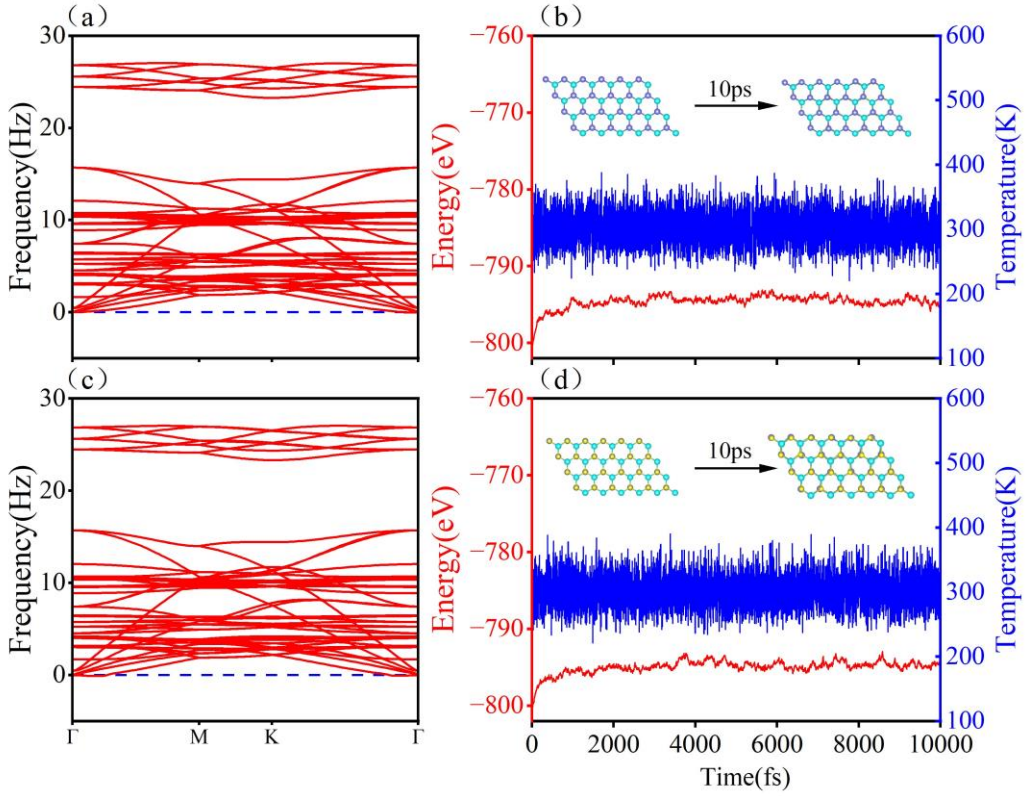


Fig. 2. (a, c) Phonon dispersion and (b, d) AIMD simulation results at 300 K for (a, b) TeWS/BP and (c, d) SWTe/BP vdWHs.

3.2 Electronic properties and optical absorptivity

Fig. 3 illustrates the interfacial electrostatic characteristics and charge transfer in TeWS/BP and SWTe/BP vdWHs, revealing the microscopic mechanisms of interfacial coupling. Figs. 3(a) and (b) plot the plane-averaged electrostatic potential perpendicular to the interface (z-axis). The narrower potential well corresponds to the BP layer, while the broader double-well feature arises from the Janus WSTe layer. The interfacial potential offset ΔV of the TeWS/BP and SWTe/BP are 1.689 eV and 1.737 eV, respectively. The slightly larger ΔV of SWTe/BP suggests a stronger intrinsic built-in electric field at its heterostructure interface, rather than stronger interlayer orbital coupling. This built-in electric field can effectively drive

the photo-generated electron-hole pairs to directionally migrate to both sides of the vdWHs, thereby suppressing carrier recombination and significantly improving the space charge separation efficiency.

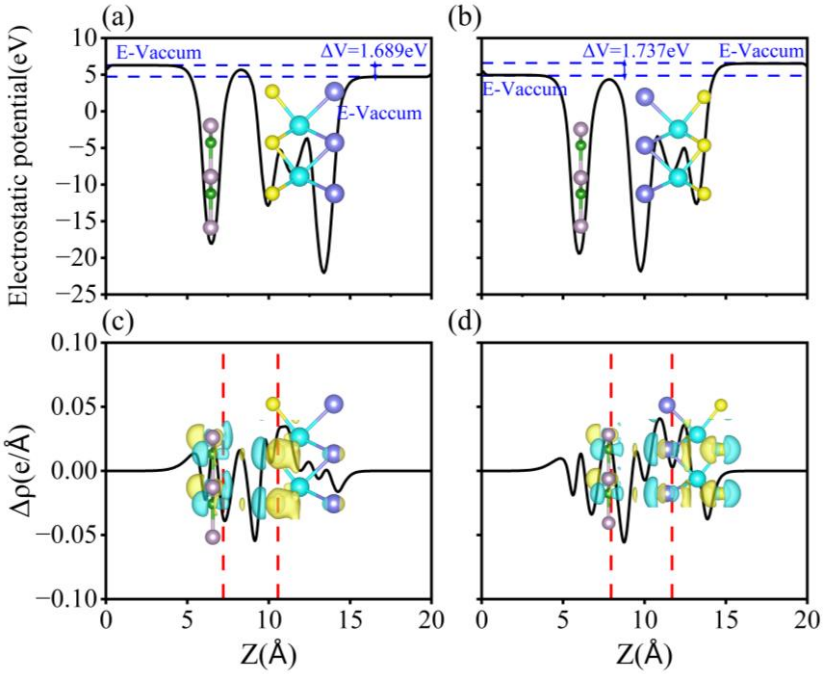


Fig. 3. Interfacial electronic properties of TeWS/BP and SWTe/BP: (a, b) Electrostatic potential profiles along the Z direction; (c, d) Plane-averaged differential charge density distributions. (a, c) TeWS/BP, (b, d) SWTe/BP. Yellow isosurfaces denote electron accumulation, cyan indicates electron depletion, and red dashed lines mark the interlayer boundaries. Isosurface values:0.0002 e/Å^3.

Figs. 3(c) and (d) plot plane-averaged differential charge density to visualize interfacial charge redistribution. Electrons transfer from BP to TeWS in TeWS/BP, while the reverse charge flow occurs in SWTe/BP. This reversed charge polarization originates from different terminal chalcogen atoms at the BP interface: sulfur (electronegativity = 2.58) contacts BP in TeWS/BP. S's stronger electronegativity extracts electrons from BP and accumulates charge on the TeWS side. For SWTe/BP, BP bonds to tellurium (electronegativity = 2.10), whose electronegativity is weaker than phosphorus (2.19). BP thus acts as an electron acceptor, drawing charge from SWTe. The disparity in electronegativity between exposed S and Te

terminals fundamentally reverses the interfacial charge transfer direction of the two heterostructures.

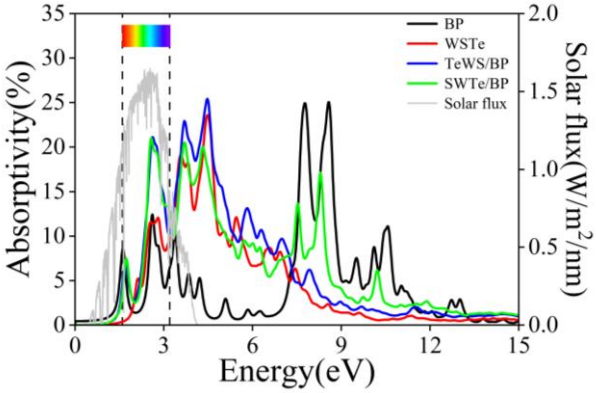


Fig. 4. Optical absorptivity of the BP, WSTe, TeWS/BP, and SWTe/BP.

Fig. 4 compares the optical absorption spectra of WSTe/BP vdWHs and their constituent monolayers. Both vdWHs exhibit markedly stronger absorption spanning the visible to ultraviolet regions compared with the isolated monolayers. Such enhanced optical absorption originates from two synergistic mechanisms: interlayer orbital hybridization generates unique cross-layer optical transitions absent in single layers [41,42]; meanwhile, the intrinsic interfacial built-in field induced by the out-of-plane dipole of Janus structures facilitates efficient separation of photogenerated carriers and further improves light-harvesting performance. Moreover, SWTe/BP achieves a maximum optical absorptivity of ~25% at around 4.5 eV, corresponding to an absorption coefficient of 1.094×10^{6} cm^{-1}, which is slightly higher than the peak absorptivity of TeWS/BP. These results verify that heterostructure engineering is an effective strategy to modulate optical properties, laying a theoretical foundation for developing high-efficiency photovoltaic materials.

3.3 Biaxial strain engineering of Janus WSTe/BP vdWHs

Strain engineering provides one of the most direct and effective routes to regulate the

physical properties of 2D materials. Biaxial strain uniformly modifies lattice constants and systematically tunes electronic structures [43–45], offering a powerful tool to understand and control the optoelectronic responses of composite systems. Fig. 5 maps the evolution of band structures under biaxial strain from −8% (compression) to +8% (tension), demonstrating the feasibility of band engineering.

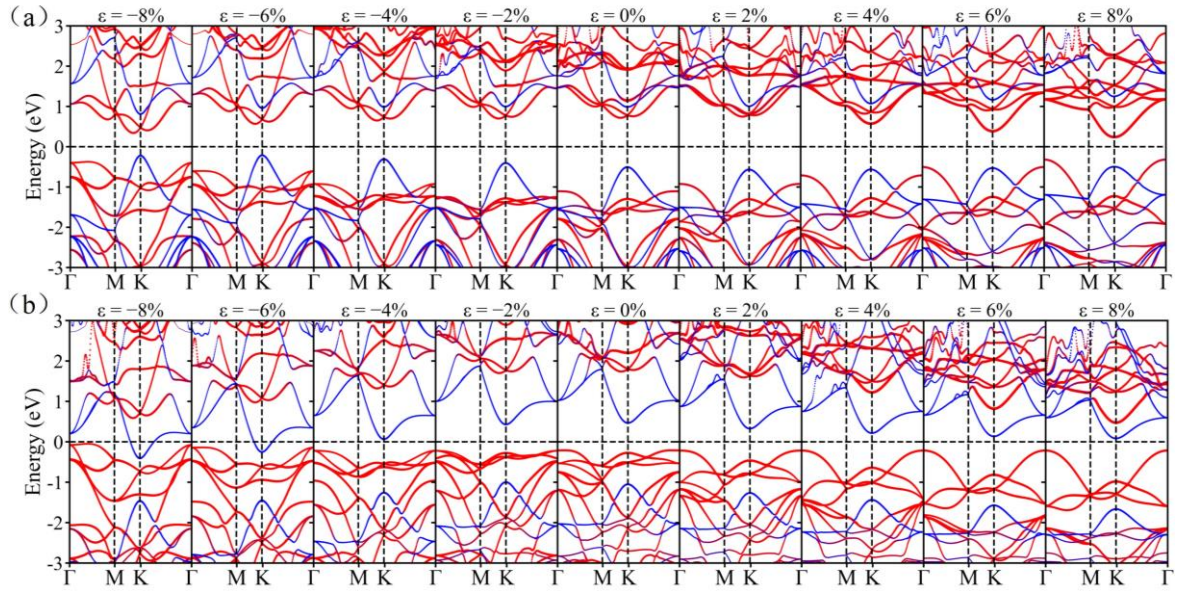


Fig. 5. Band structures of (a) TeWS/BP and (b) SWTe/BP under biaxial strain from –8% to +8%. Blue lines denote the BP layer, and red lines denote the Janus WSTe monolayer.

To verify whether the ±8% biaxial strain remains within the elastic deformation regime of the heterostructures, we additionally calculated the elastic stiffness matrices of the TeWS/BP and SWTe/BP heterostructures under ±8% strain, the corresponding results are summarized in Table 1. As well as their stress–strain curves under biaxial strain ranging from −8% to +8% (as shown in Fig. 6).

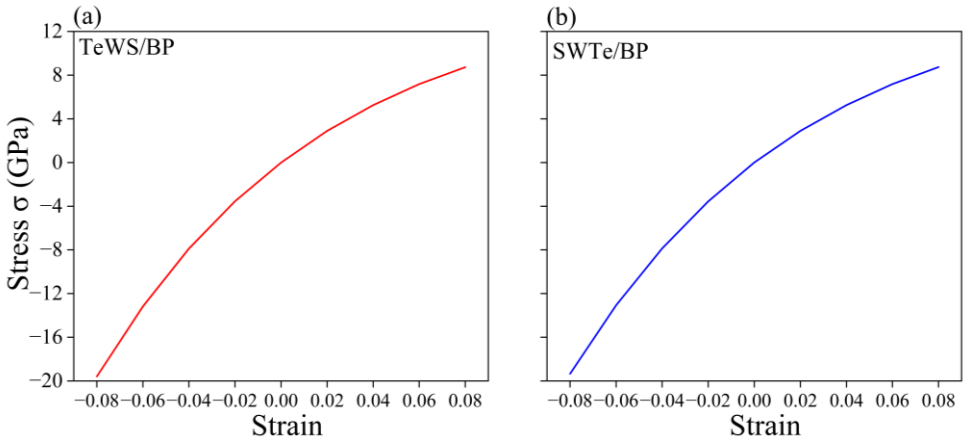


Fig. 6. Stress–strain curves of the TeWS/BP (a) and SWTe/BP (b) heterostructures under biaxial strain ranging from −8% to +8%.

Table 1 Elastic stiffness coefficients (C_{11} C_{22} C_{12} C_{66}) of the heterostructures.

Heterostructure	C_{11}(GPa)	C_{22}(GPa)	C_{12}(GPa)	C_{66}(GPa)
TeWS/BP (8%)	78.60	78.40	12.97	32.77
TeWS/BP (–8%)	224.94	227.38	57.65	84.92
SWTe/BP (8%)	78.59	78.66	13.56	32.58
SWTe/BP (–8%)	192.75	198.10	82.47	51.36

Elastic stiffness coefficients C_{ij} quantify material resistance against elastic deformation: C_{11} and C_{22} describe in-plane axial deformation resistance, while C_{66} characterizes shear-deformation resistance. All computed elastic constants satisfy the Born-Huang mechanical-stability criteria. Combined with continuous, non-abrupt stress-strain responses across −8 % ~ +8 % biaxial strain in Fig. 6, we confirm that both heterostructures stay mechanically stable at this maximum strain magnitude. Therefore, the ±8 % strain window lies within a mechanically stable deformation regime. These results provide a solid mechanical foundation for our subsequent strain-tunable electronic and optoelectronic property discussions.

Fig. 5 (a) illustrates the strain-dependent band structure evolution of TeWS/BP. Under zero strain (ε = 0%), the system exhibits a typical type-II band alignment with an indirect bandgap. As tensile strain increases, the conduction band minimum (CBM) shifts toward the Fermi level, leading to a band alignment transition to type-I at +6% strain. This transition arises physically from strain-induced modifications in interlayer coupling strength and the degree of lattice symmetry breaking. In contrast, compressive strain monotonically reduces the bandgap, which narrows sharply at −8% and trends toward metallic character. Fig. 5 (b) presents the strain response of the SWTe/BP. In marked contrast to TeWS/BP, SWTe/BP retains a type-II band alignment across the entire strain range from –4% to +8%, while transitioning to a metallic state at –8% and –6%. This difference originates from the distinct orientation of the interfacial dipole moment in the two stacking configurations: in SWTe/BP, the interfacial electric field couples only weakly with the strain-induced deformation field, limiting the ability to alter the spatial distribution of charge carriers. Meanwhile, the band gap of the SWTe/BP presents an approximately linear strain-dependent relationship: it gradually decreases under tensile strain and closes much more rapidly under compressive strain. Blue and red orbital contributions indicate BP and WSTe characters, respectively. During strain modulation, layer-resolved band edges shift markedly while interlayer orbital hybridization remains relatively stable, confirming that strain mainly regulates band-edge energies rather than intrinsic orbital hybridization. Such evolution has critical implications for photovoltaic applications. TeWS/BP can switch between type-II and type-I alignments under moderate tensile strain (+6% to +8%), enabling tailored carrier separation. In contrast, the robust type-II character of SWTe/BP ensures efficient carrier separation even under fluctuating strains. The

complementary properties of the two stacking configurations provide a reliable materials platform for strain-adaptive photovoltaic devices.

Fig. 7 plots band-edge energies and strain-induced band-alignment evolution for the two heterostructures. Fig.7(a) shows band edges for SWTe/BP: BP band edges (blue) depend weakly on strain, while WSTe edges (red) vary more strongly. Under strong compression (−8%, −6%), the gap closes and the system become metallic. For strains above −4%, the WSTe CBM shifts upward, stabilizing type-II alignment. The Fermi level (dashed line) marks the transition from degenerate to semiconducting behavior. In contrast, TeWS/BP (Fig. 7(b)) shows more complex evolution: BP band edges vary monotonically with strain, while the WSTe CBM reaches a minimum near −2% strain due to strain-modified orbital hybridization. Band crossing near the Fermi level suggests possible semimetallic behavior or band inversion.

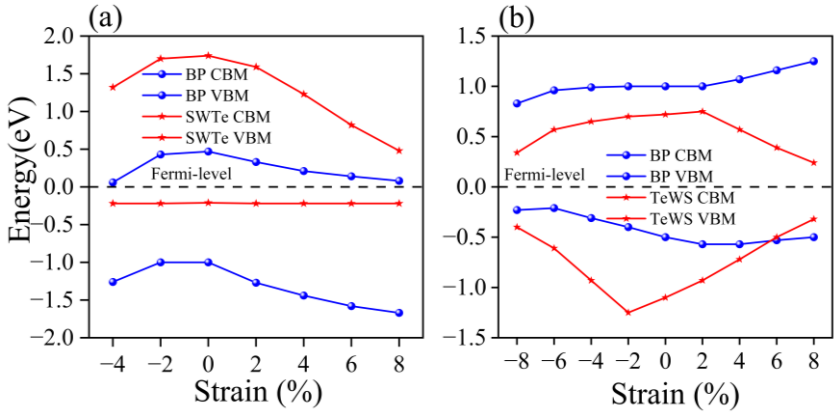


Fig. 7. Strain-dependent band-edge evolution for (a) SWTe/BP and (b) TeWS/BP.

Fig. 8 shows the band-edge evolution relative to the vacuum level. For each heterostructure, the stable plateau of planar-averaged electrostatic potential in the sufficiently distant vacuum region was taken as the vacuum level E_{vac}. The valence-band maximum (VBM) and conduction-band minimum (CBM) were referenced against this system-specific vacuum level using: $E_{VBM}^{Vac} = E_{VBM} - E_{Vac}$, and $E_{CBM}^{Vac} = E_{CBM} - E_{Vac}$. Consequently, all

reported band-edge positions adopt the vacuum plateau computed from each individual supercell as the unified energy reference. No separate reference slab or macrodipole correction was applied.

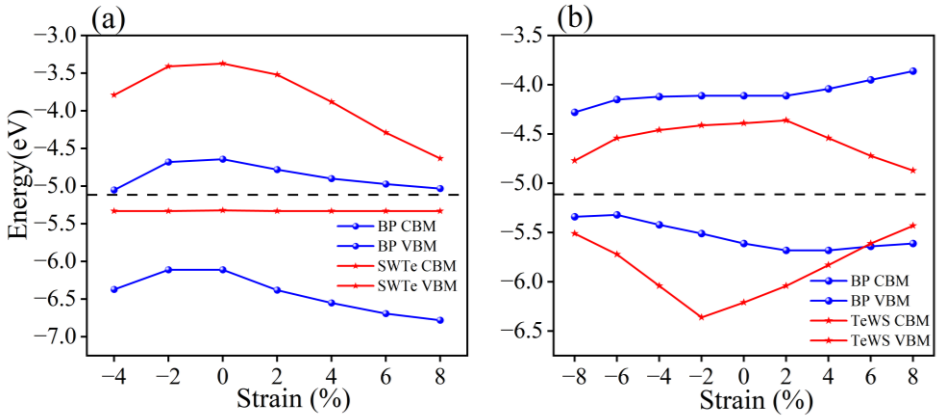


Fig. 8. Strain-dependent absolute band-edge evolution for (a) SWTe/BP and (b) TeWS/BP.

Fig. 9 summarizes strain-induced band-alignment phase diagrams. SWTe/BP becomes metallic below −6% strain and maintains stable type-II semiconducting character from −6% to +8%. In comparison, TeWS/BP retains a finite gap across the full strain range: it shows type-II alignment from −8% to +4%, with a maximum gap of 1.32 eV at +2% tension, corresponding to optimal PCE. Beyond +4% tension, the gap drops abruptly and the alignment switches to type-I. Under strong tension, the WSTe CBM falls below the BP CBM, confining carriers within a single layer and disabling spatial separation. A comparison reveals that stacking geometry controls strain response: SWTe/BP uses a strong interfacial dipole to lock type-II alignment, ideal for flexible devices. In contrast, the weaker dipole in TeWS/BP enables strain-tunable alignment transitions. Moderate +2% tension in TeWS/BP simultaneously yields a large gap and type-II alignment, making it favorable for high-efficiency photovoltaics. These findings establish key design rules for strain-adaptive optoelectronic devices.

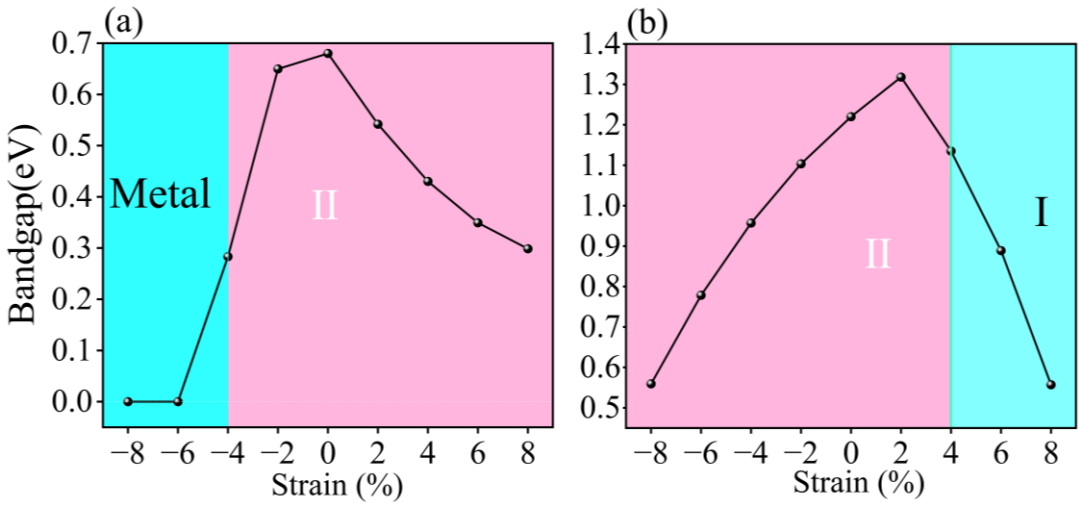


Fig. 9. Strain-induced band alignment phase diagrams for (a) SWTe/BP and (b) TeWS/BP.

Fig. 10 (a, b) show strain-tunable optical absorptivity curves of TeWS/BP. Under compression (−8% to 0%), the absorption edge redshifts noticeably, while visible-range (1.5–3.0 eV) peak intensities decrease overall with peak splitting and broadening. These features arise from strain-lifted band degeneracy and density-of-states redistribution. Under tension (0% to +8%), the edge blueshifts more gradually than under compression. Figs 10(c) and (d) display corresponding results for SWTe/BP. Under compression, the edge also redshifts, but peak profiles remain more stable with milder intensity reduction, indicating greater optical robustness against compression. Under tension, the edge progressively blueshifts, reaching ~1.5 eV at +8%. Unlike TeWS/BP, SWTe/BP shows non-monotonic absorption peaks (rising then falling), with a broad plateau from +4% to +6%. The two heterostructures exhibit configuration-dependent optical strain responses: TeWS/BP shows enhanced visible absorption at +2% tension, while SWTe/BP maintains robust absorption over a wide strain window. This difference arises from distinct strain-tuning mechanisms: alignment transitions in TeWS/BP alter optical selection rules, while stable type-II alignment in SWTe/BP preserves transition channels. These results provide a quantitative basis to optimize light harvesting in

2D photovoltaic materials via strain engineering.

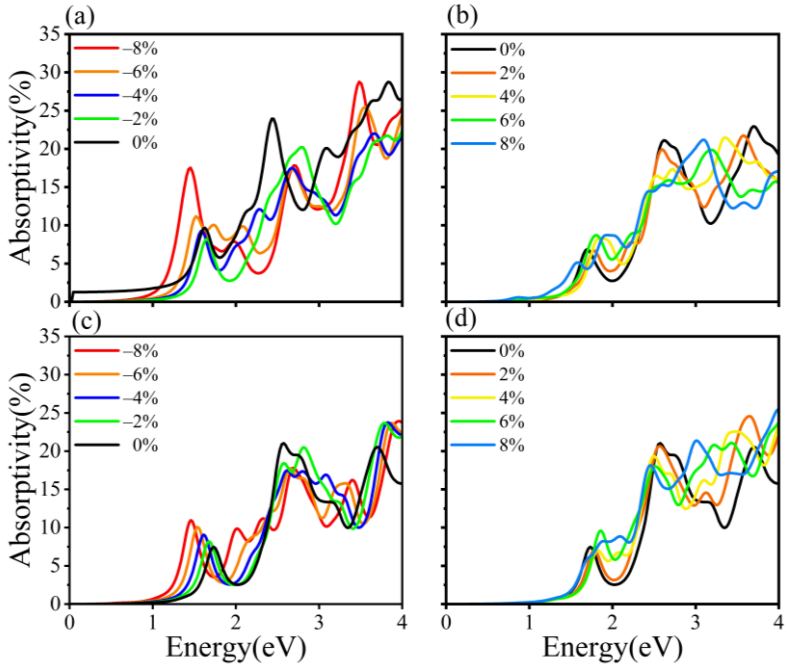


Fig. 10. Optical absorptivity under biaxial strain: (a, c) compressive strain; (b, d) tensile strain for (a, b) TeWS/BP and (c, d) SWTe/BP.

In direct-gap materials, VBM and CBM locate at identical k-points; photons with negligible crystal momentum can trigger vertical optical transitions. For indirect-band-gap systems, VBM and CBM sit at distinct k-points; fundamental-gap optical transitions require phonon assistance to satisfy momentum conservation. Hence the fundamental Kohn-Sham band gap does not guarantee strong optical absorption near the band edge. Our PCE evaluation adopts the idealized Shockley-Queisser (SQ) framework, which takes the fundamental band gap as the photon-absorption threshold. This built-in approximation assumes step-like optical absorption at the band-gap energy and does not explicitly incorporate phonon-assisted transitions, electron-phonon coupling, or real absorption-coefficient spectra. For indirect-gap heterostructures, real-world photocurrent and practical PCE may be lower than SQ theoretical limits due to weakened band-edge

phonon-assisted absorption. However, the SQ model itself does not internally downgrade theoretical efficiency purely because of an indirect band gap; deviations originate from non-ideal absorption behavior outside the SQ model's assumptions. Accordingly, the PCE values reported in this work represent theoretical predictions under unified ideal SQ assumptions, and are primarily intended for comparing relative photovoltaic performance among different heterostructures. They should not be interpreted as realistic device efficiencies that fully account for phonon-mediated optical processes.

Table 2 summarizes the photovoltaic performance parameters of the TeWS/BP and SWTe/BP heterostructures under biaxial strain, including the donor bandgap (E_{gd}), conduction band offset (ΔE_c), and PCE. TeWS/BP exhibits outstanding photovoltaic response. The PCE stays above 19% from −2% to +2% strain, peaking at 20.98% under +2% tension. However, TeWS/BP PCE is strain-sensitive and degrades rapidly outside this window. Under −8% compression, PCE falls to 8.02%, mainly due to lattice-distortion-induced non-radiative recombination channels. At +4% strain, although the gap widens further, the conduction-band offset increases to 0.50 eV; the excessive barrier height aggravates energy loss and reduces PCE to 16.38%. In contrast, SWTe/BP shows much poorer photovoltaic performance. At zero strain, PCE is only 5.26% and remains below 6% across the accessible strain range. This bottleneck stems from an intrinsic band-structure drawback: the conduction-band offset reaches 1.27 eV, far beyond the optimal 0.2–0.4 eV window for high-performance photovoltaics. Such a large offset creates a strong energy barrier for electron injection and severely suppresses interfacial carrier transport. Notably, strain weakly modulates this offset, which stays near 1.26–1.27 eV from −4% to +2% strain, locking PCE at low levels. Under

strong tension (+6%), the offset decreases to 0.68 eV, but the gap narrows to 1.04 eV, increasing thermal relaxation losses and further lowering PCE to 1.82%. These results reveal a fundamental mismatch between the interfacial field orientation in SWTe/BP and efficient carrier separation. Collectively, these findings establish key design principles for Janus-heterostructure photovoltaics: interfacial atomic arrangement determines band-alignment type and directly controls strain-tunable PCE via interfacial dipole strength.

Table 2 Photovoltaic performance parameters of TeWS/BP and SWTe/BP under biaxial strain, including donor bandgap (E_{gd}), conduction band offset (ΔE_c), and power conversion efficiency (PCE). The "×" symbol indicates that under these strain conditions, no open-circuit voltage can be generated, and thus the PCE value cannot be obtained.

vdWH		–8%	–6%	–4%	–2%	0%	2%	4%	6%	8%
TeWS/BP	E_{gd} (eV)	1.06	1.17	1.30	1.40	1.50	1.57	1.64	0.89	0.56
	ΔE_c (eV)	0.49	0.39	0.34	0.30	0.28	0.25	0.50	0.77	0.49
	PCE (%)	8.02	13.73	16.98	19.31	20.40	20.98	16.38	×	×
SWTe/BP	E_{gd} (eV)	×	×	1.54	1.92	1.95	1.81	1.45	1.04	0.70
	ΔE_c (eV)	×	×	1.26	1.27	1.27	1.26	1.02	0.68	0.40
	PCE (%)	×	×	×	5.21	5.26	4.21	3.04	1.82	×

3.4 Photogalvanic Effect in Janus WSTe/BP photodetector

Fig. 11 illustrates Janus WSTe/BP photodetector architectures. Panels (a,b) show symmetric contacts using the heterostructure for both electrodes; panels (c,d) depict asymmetric designs with BP left electrodes and WSTe right electrodes to avoid spurious interlayer effects reported in earlier work [26,46]. Device setups for TeWS/BP and SWTe/BP are analogous, with channels along zigzag and armchair directions. After achieving static self-consistency under zero bias, linearly polarized light is applied to the central scattering

region for photo-excitation, and the photo-generated electron–hole pairs undergo spatial separation, thereby forming a detectable photocurrent signal. To characterize visible-light response, photon energy is swept from 1.6 to 4.0 eV in 0.1 eV steps, and polarization angles vary from 0° to 180° in 15° steps. Given structural similarities, we use SWTe/BP as representative to illustrate detailed contact characteristics.

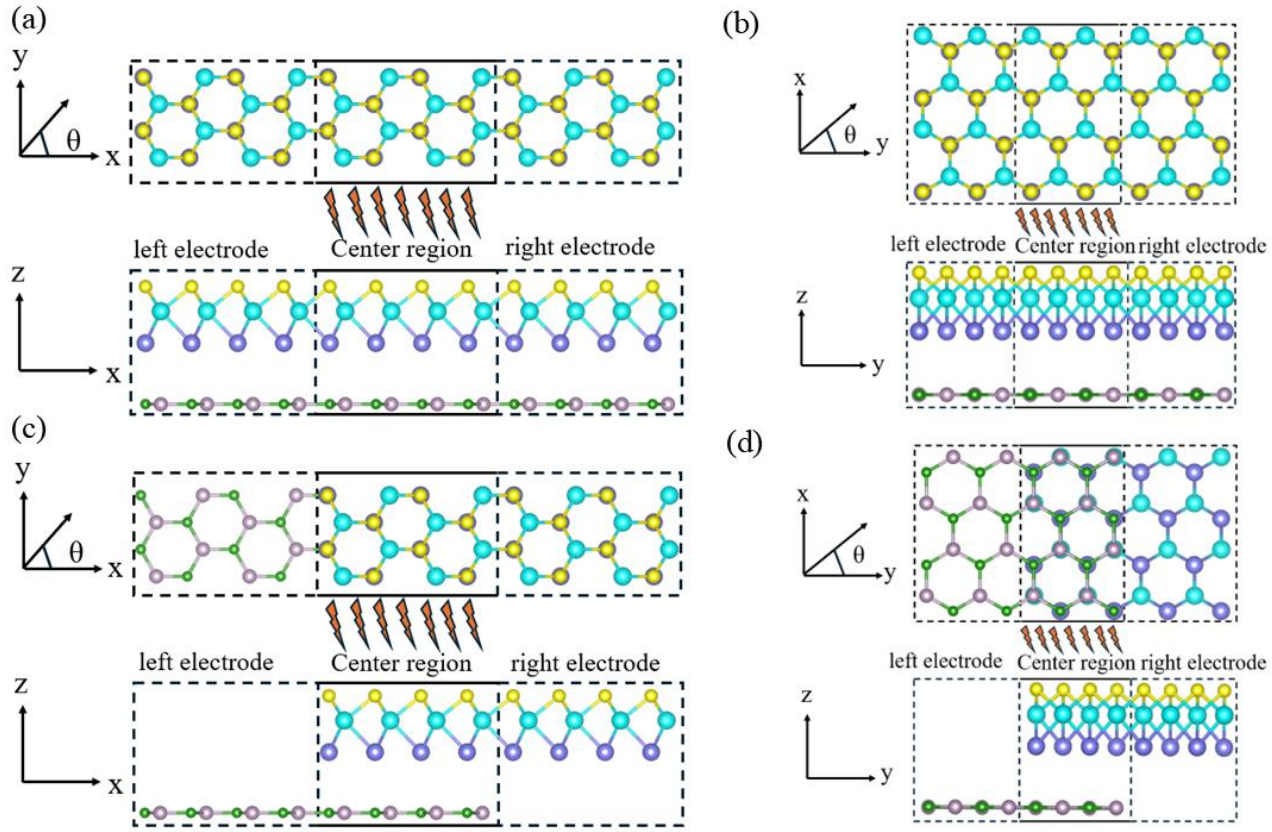


Fig. 11. Device structures of Janus WSTe/BP photodetectors: (a, c) armchair direction, (b, d) zigzag direction; (a, b) symmetric electrode contacts, (c, d) asymmetric electrode contacts.

Figs. 12 and 13 present the photocurrent response characteristics of Janus WSTe/BP heterostructure photodetectors under different electrode configurations: Fig. 12 for symmetric contacts and Fig. 13 for asymmetric contacts. The results are presented as three-dimensional surface plots illustrating the photocurrent as a function of photon energy and polarization angle. As shown in Fig. 12, In the symmetric contact configuration, the maximum

photocurrent (I_{Max}) of TeWS/BP along the armchair direction is only 0.05 a_0^2/photon, indicating a generally weak response. Along the zigzag direction, however, a pronounced directional anisotropy emerges, with the I_{Max} reaching 0.18 a_0^2/photon at approximately 2.5 eV and a polarization angle of 90°. In stark contrast, the SWTe/BP symmetric contact exhibits markedly different behavior. Along the armchair direction, the photocurrent is significantly enhanced, achieving a maximum of 2.34 a_0^2/photon at 2.8 eV and 90°, along with a secondary peak at 3.8 eV, yielding an overall response an order of magnitude higher than that of TeWS/BP. Along the zigzag direction, the I_{Max} is 1.57 a_0^2/photon, slightly lower than that along the armchair direction. This strong anisotropy is closely related to the type-II band alignment and interfacial electric field distribution in SWTe/BP.

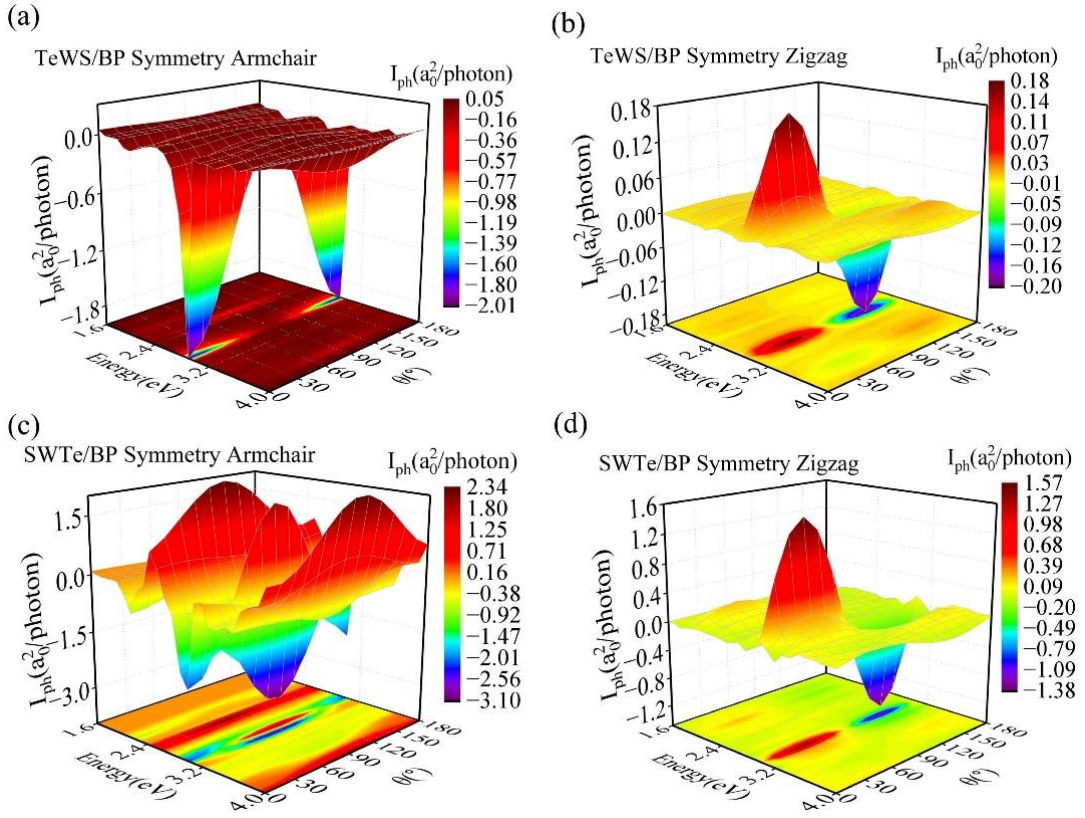


Fig. 12. 3D contour maps of polarization-dependent photocurrent for symmetric-contact Janus WSTe/BP photodetectors: (a, c) armchair direction, (b, d) zigzag direction, (a, b) TeWS/BP, (c, d) SWTe/BP.

As shown in Fig. 13, breaking inversion symmetry via asymmetric contacts greatly enhances the PGE, converting the weak responses observed in symmetric configurations into substantially amplified photocurrents [47,48]. For the TeWS/BP asymmetric contact device, the I_{Max} along the armchair direction increases dramatically to 17.95 a_0^2/photon — approximately 360 times that of its symmetric counterpart along the same direction. Along the zigzag direction, TeWS/BP reaches a I_{Max} of 24.19 a_0^2/photon, notably achieving the optimal photoresponse among the WSTe/BP devices. For SWTe/BP in the asymmetric configuration, the I_{Max} along the zigzag direction is 17.61 a_0^2/photon, comparable to that of TeWS/BP along the armchair direction. Along the armchair direction, the asymmetric contact yields a I_{Max} of approximately 6.94 a_0^2/photon for SWTe/BP, which is three times that of its symmetric configuration.

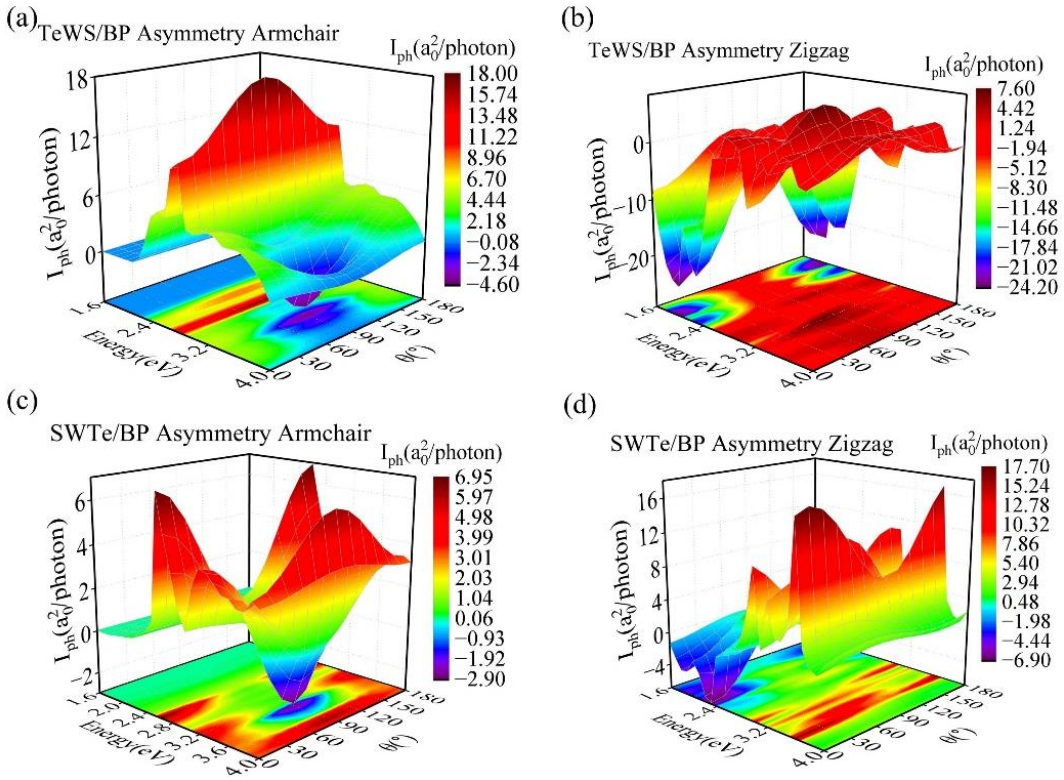


Fig. 13. 3D contour maps of polarization-dependent photocurrent for asymmetric-contact Janus WSTe/BP photodetectors: (a, c) armchair direction, (b, d) zigzag direction, (a, b) TeWS/BP, (c, d) SWTe/BP.

The results demonstrate that the contact configuration significantly influences the photoresponse of heterostructure photodetectors. In the symmetric contact geometry, the photocurrent is constrained by the symmetric distribution of the built-in electric field, resulting in low carrier separation efficiency. In contrast, the asymmetric contact introduces an additional potential gradient that breaks spatial symmetry, enhancing the photocurrent by one to two orders of magnitude. This enhancement is particularly pronounced along specific crystallographic directions—armchair for TeWS/BP and zigzag for SWTe/BP—offering a promising route for designing high-sensitivity polarization-sensitive photodetectors.

Figs. 14 and 15 present 2D photocurrent maps for symmetric and asymmetric contacts at photon energies of 1.6 eV, 2.8 eV, and 4.0 eV. The symmetric contact configuration exhibits a weak photocurrent response and weak polarization dependence. The results show that the photocurrent along the zigzag direction can be well described by $\alpha\sin(2\theta) + I_0$, while that along the armchair direction follows $\beta\cos(2\theta) + I_0$, in excellent agreement with the theory of the PGE [49].

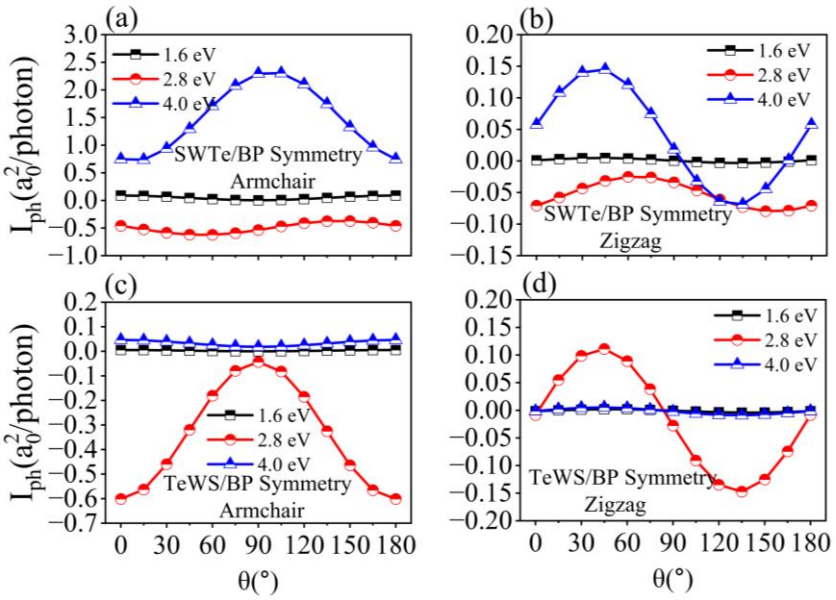


Fig. 14. Polarization-resolved photocurrent of symmetric-contact Janus WSTe/BP photodetectors: (a, c)

armchair direction, (b, d) zigzag direction, (a, b) SWTe/BP, (c, d) TeWS/BP.

Owing to the reduced symmetry of the asymmetric contact configuration, some curves exhibit an initial phase shift, consistent with previous reports [50–53]. Moreover, as the photon energy increases, the photocurrent generated along different crystallographic directions increases to varying degrees compared with that under 1.6 eV irradiation. The photocurrent again follows the form $\alpha\sin(2\theta) + I_0$ along the zigzag direction and $\beta\cos(2\theta) + I_0$ along the armchair direction, in agreement with the theory of the PGE.

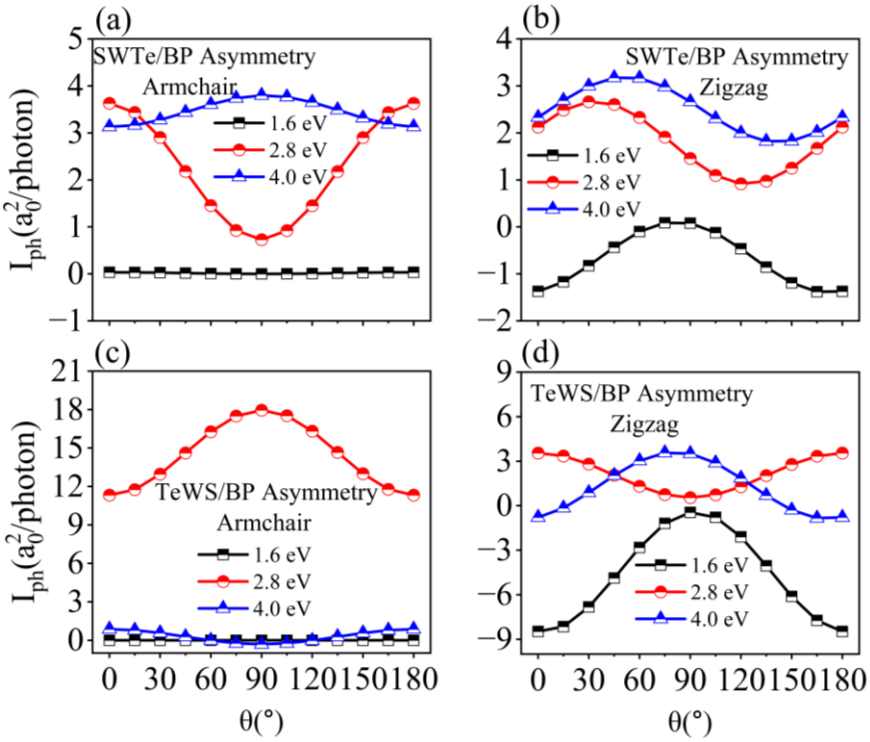


Fig. 15. Polarization-resolved photocurrent of asymmetric-contact Janus WSTe/BP photodetectors: (a, c) armchair direction, (b, d) zigzag direction, (a, b) SWTe/BP, (c, d) TeWS/BP.

For a direct comparison of photocurrent intensities, Fig. 16 presents the variation in I_{Max} with photon energy. The results show that the I_{Max} achieved by the SWTe/BP photodetector is comparable to that of the TeWS/BP heterostructure. Further comparison of their anisotropy reveals that SWTe/BP exhibits a strong direction-dependent response across different photon energies, with I_{Max} along the armchair direction significantly exceeding that

along the zigzag direction. In contrast, the TeWS/BP heterostructure shows a much smaller difference in I_{Max} between the armchair and zigzag directions across the same energy range.

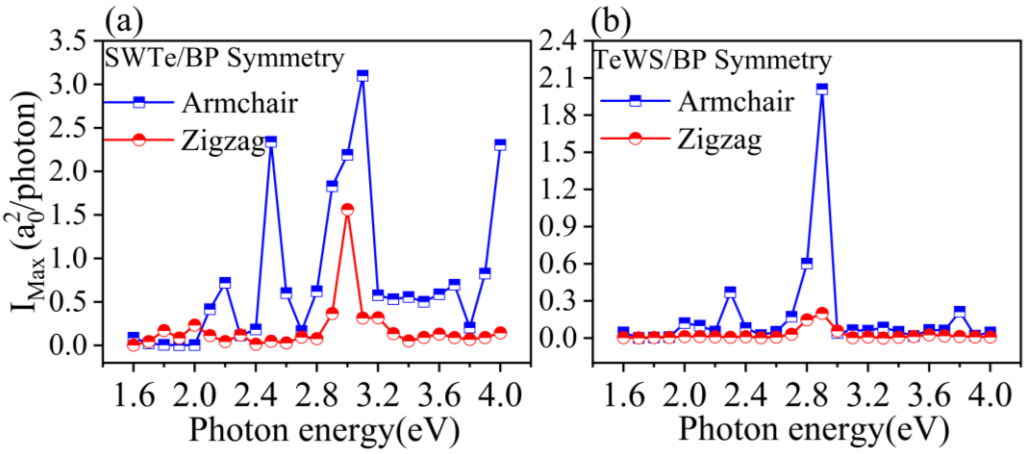


Fig. 16. Maximum photocurrent of symmetric-contact Janus WSTe/BP photodetectors: (a) SWTe/BP, (b) TeWS/BP.

To elucidate the mechanism underlying the I_{ph} peaks, the total density of states (TDOS) in the central region of symmetric-contact SWTe/BP and TeWS/BP photodetectors was calculated. As shown in Fig. 17, the generation of I_{Max} is governed by electronic transitions from the valence band (VB) to the conduction band (CB). In accordance with Fermi's golden rule, the transition probability is proportional to the DOS [35,36]. For the SWTe/BP photodetector, two distinct DOS feature pairs are observed. The VB peak at −0.50 eV and the CB peak at 2.51 eV result in a markedly enhanced transition probability within this energy range, explaining the pronounced I_{Max} observed under 3.1 eV illumination along the armchair direction—consistent with the data presented in Fig. 16. The second feature pair, consisting of a VB peak at −0.36 eV and a CB peak at 2.68 eV, similarly promotes electronic transitions upon 3.0 eV photon absorption, giving rise to a significant photocurrent in the zigzag direction. For the TeWS/BP photodetector, the DOS exhibits two pairs of VB-CB features at (−1.00 eV, 1.90 eV), corresponding to the zigzag and armchair orientations, respectively. Absorption of 2.9 eV photons drives photocurrent generation in both directions, and all variations in I_{Max} shown in Fig. 16 can be consistently accounted for by the

aforementioned DOS characteristics.

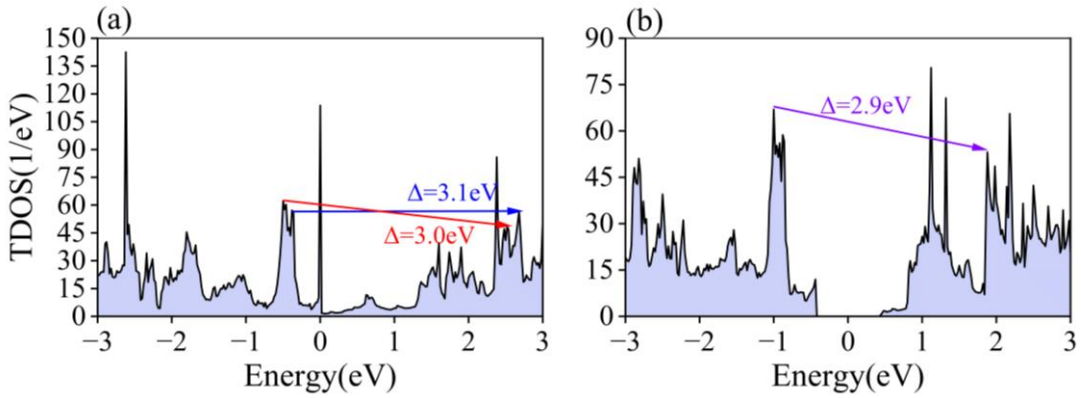


Fig. 17. Total density of states in the central region of (a) SWTe/BP and (b) TeWS/BP photodetectors.

Fig. 18 shows polarization extinction ratio (ER) as a function of photon energy for symmetric-contact devices. The extinction ratio (ER) is the core metric to quantify the polarization discrimination ability of photodetectors, defined as the ratio between photocurrents collected under two orthogonal polarized light ($R_{//}/R_{\perp}$ or $R_{\perp}/R_{//}$). Larger ER values correspond to stronger polarization sensitivity of the device. As shown in Fig. 18(a), SWTe/BP along armchair yields an exceptionally high ER, peaking at ~155.5 at 3.1 eV, arising from large differences between parallel and perpendicular polarized responses, indicating strong polarization-dependent photocurrent modulation. Along zigzag (Fig. 18(b)), SWTe/BP peaks at ~59.9 at 1.7 eV, with a secondary peak of 49.2 at 3.5 eV; this multi-peak behavior indicates distinct polarization selectivity for different transition energies. For TeWS/BP along armchair (Fig. 18(c)), ER peaks at 58.0 at 1.9 eV, with a second peak of 34.7 at 2.9 eV, showing a gentler overall trend than SWTe/BP. Along zigzag (Fig. 18(d)), TeWS/BP peaks at ~38.3 at 1.8 eV, indicating relatively weaker polarization sensitivity. Under symmetric contacts, both heterostructures show clear energy-dependent ER; however, SWTe/BP exhibits stronger overall polarization sensitivity, closely linked to its more anisotropic photocurrent response.

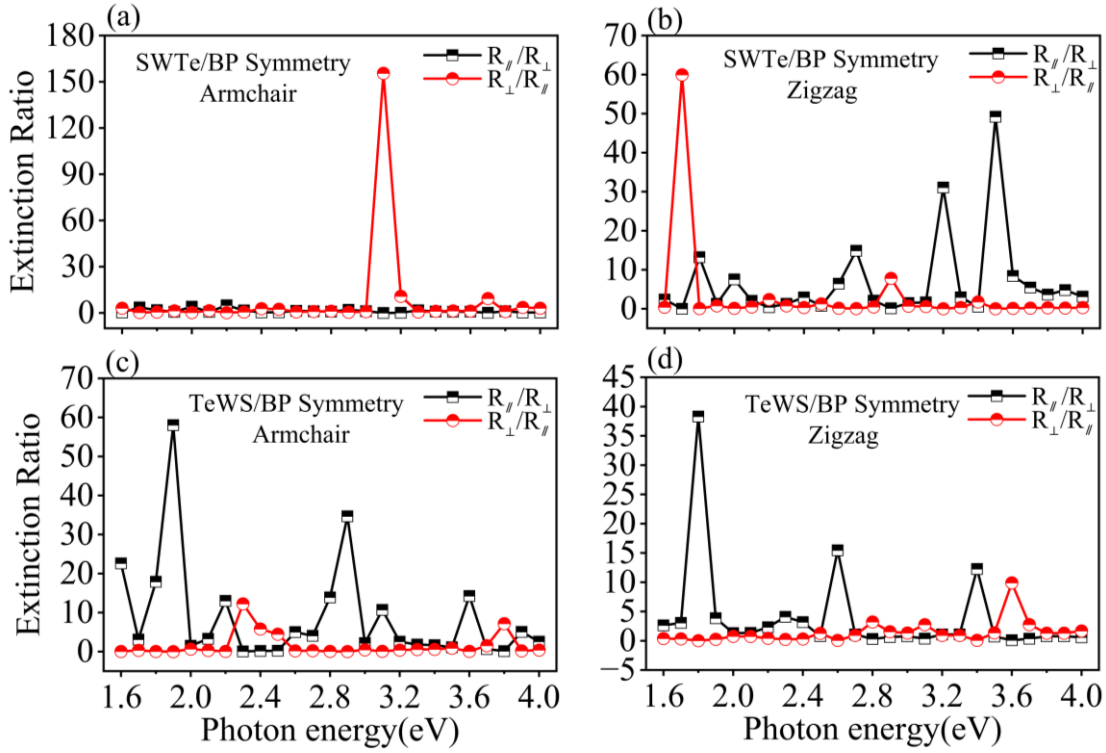


Fig. 18. Extinction ratio of symmetric-contact Janus WSTe/BP photodetectors.

Fig. 19 illustrates the polarization extinction ratio performance of devices with asymmetric electrode contacts. As shown in Fig. 19(a), ER for SWTe/BP along armchair jumps to ~109.6 at 1.8 eV, about 4.5 times higher than under symmetric contacts, arising from broken spatial inversion symmetry induced by asymmetric electrodes. Along zigzag (Fig. 19(b)), SWTe/BP similarly peaks at ~121.6 at 1.8 eV. TeWS/BP along armchair shows a striking multi-peak response, reaching 327.2 and 317.3 at 1.9 eV and 2.1 eV, respectively (Fig. 19(c)); this double-peak feature reflects complex band structure near the infrared-visible crossover. Along zigzag, TeWS/BP peaks at 200.9 at 2.2 eV (Fig. 19(d)). Asymmetric contacts enhance ER by nearly an order of magnitude, attributed to strong built-in fields from asymmetric electrodes that efficiently separate photocarriers while breaking centrosymmetry to produce a cleaner polarization response.

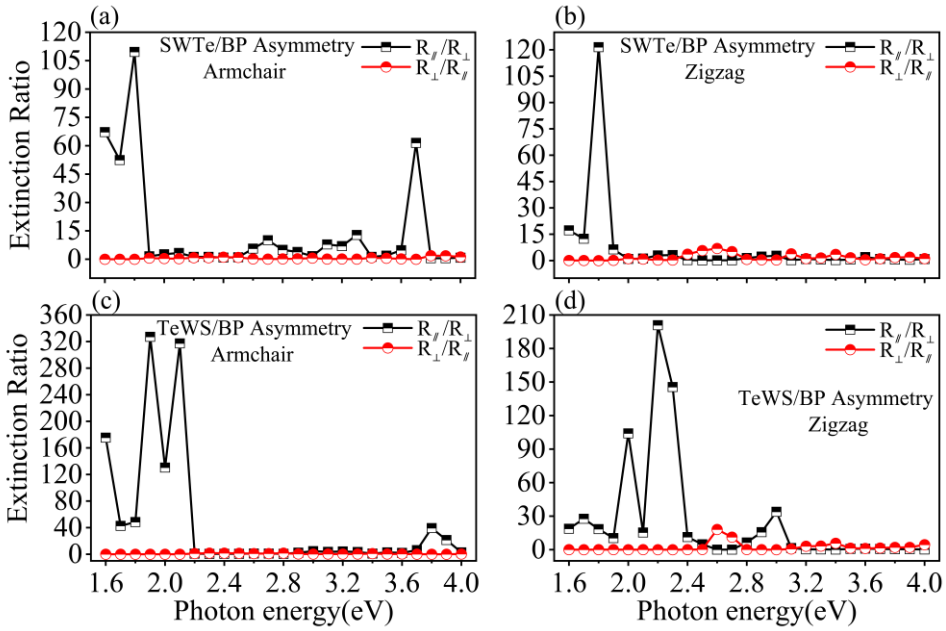


Fig. 19. Extinction ratio of asymmetric-contact Janus WSTe/BP photodetectors

4. Conclusion

We systematically investigate the strain-tunable optoelectronic properties of Janus WSTe/BP vdWHs through first-principles calculations. Two most stable stacking configurations, TeWS/BP and SWTe/BP, both feature intrinsic type-II band alignment. Visible-range optical absorption is strongly enhanced relative to the component monolayers. Stacking geometry dominates the strain response of band alignment: TeWS/BP, with a weaker interfacial dipole, undergoes strain-driven band-alignment transitions, whereas SWTe/BP, with a stronger interfacial dipole, retains stable type-II alignment. TeWS/BP vdWH achieves a peak PCE of 20.98% under +2% tensile strain and maintains PCE above 19% from −2% to +2% strain. Furthermore, electrode engineering provides an effective strategy to boost photodetection performance. Using asymmetric contacts to break spatial inversion symmetry, the photocurrent is drastically enhanced from ~2.0 a_0^2/photon (symmetric) up to 18.0 a_0^2/photon, greatly improving detection sensitivity. These findings provide quantitative

design principles and technical guidance for band engineering and performance optimization in Janus-heterostructure optoelectronic devices, highlighting the great potential of Janus WSTe/BP systems for next-generation photovoltaics and high-sensitivity polarization-resolved photodetection.

Conflicts of interest

The authors declare no conflicts of interest.

Acknowledgments

This work was supported by the Natural Science Basic Research Program of Shaanxi (Grant No. 2025JC-YBMS-065).

References

[1] Yeh C H 2020 *ACS Omega* **5** 31398

[2] Xu H Q, Xiao G and Xiao W Z 2022 *Micro Nanostruct.* **170** 207396

[3] Xiao Y, He S and Fan X 2024 *J. Alloys Compd*. **1006** 176358

[4] Jiang Y, Lei S and Wang M 2024 *ACS Appl. Mater. Interfaces* **16** 30521

[5] Wang S D, Li J Y and Wang Y H 2026 *Chin. Phys. B* **35** 027502

[6] Luo R H, Liu S Y and Dong X 2026 *Chin. Phys. B* **35** 034201

[7] Wang Z, Gong C and Zhang C 2025 *DeCarbon* **8** 100107

[8] Liu Q S, Yu J H and Hu J B 2024 *Chin. Phys. B* **33** 017204

[9] Xie Y, Jiang N N and Han W 2024 *J. Phys. Chem. Solids* **192** 112067

[10] Zhou B, Cui A and Gao L 2021 *Phys. Rev. Mater*. **5** 125404

[11] Liu J, Ma N and Wu W 2020 *Chem. Eng. J*. **393** 124719

[12] Qi Y X, Zhao J and Zeng H 2024 *Chin. Phys. B* **33** 096302

[13] Babariya B, Gupta S K and Gajjar P N 2023 *Surf. Interfaces* **42** 103409

[14] Zhao H and Lam J C K 2025 *Crystals* **15** 567

[15] Kar S, Kumari P and Kamalakar M V 2023 *Sci. Rep*. **13** 13696

[16] Amirian S, Fatahi N and Naseri M 2025 Mater. *Today Commun*. **42** 111217

[17] Meng L, Huang Q and Liu C 2021 *Chem. Phys. Lett*. **781** 138989

[18] Cakmak N, Kadioğlu Y and Gökoğlu G 2020 *Philos. Mag. Lett*. **100** 116

[19] Wang S and Wu X 2015 *Chin. J. Chem. Phys*. **28** 588

[20] Zhuang H L and Hennig R G 2012 *Appl. Phys. Lett*. **101** 153109

[21] Khang N D, Nguyen C Q and Duc L M 2023 *Nanoscale Adv*. **5** 2583

[22] Ou Z, Zheng Y J and Pan Y 2025 *J. Phys. Chem. Lett.* **16** 10324

[23] Li M Z, Zhang M L and Ji X Q 2026 *Chin. Phys. B* **35** 028502

[24] Xiao X S, Xie Y and Zhang M 2026 *J. Phys. Chem. Solids* **209** 113284

[25] Han W, Xie Y and Hao J Y 2025 *Diamond Relat. Mater*. **152** 111965

[26] Shi M, Lv Y and Wu G 2024 *ACS Appl. Mater. Interfaces* **16** 22622

[27] Kresse G and Furthmüller J 1996 *Phys. Rev. B* **54** 11169

[28] Hafner J 2008 J. Comput. Chem. **29** 2044

[29] Bučko T, Hafner J and Lebègue S 2010 *J. Phys. Chem*. A **114** 11814

[30] Kresse G and Joubert D 1999 *Phys. Rev. B* **59** 1758

[31] Heyd J and Scuseria G E 2004 *J. Chem. Phys*. **120** 7274

[32] Perdew J P, Burke K and Ernzerhof M 1996 *Phys. Rev. Lett*. **77** 3865

[33] Chadi D J 1977 *Phys. Rev. B* **16** 1746

[34] Waldron D, Haney P and Larade B 2006 *Phys. Rev. Lett*. **96** 166804

[35] Xie Y, Chen Z Y and Jin X W 2025 *Physica B* **717** 417775

[36] Cui Z, Zhang G and Zhang S 2024 *Micro Nanostruct.* **193** 207922

[37] Qi X, Li E and Shen Y 2025 *Surf. Interfaces* **58** 105783

[38] El Hamdaoui J, Pérez L M and Ojeda-Martínez M 2023 *Nanomaterials* **13** 2535

[39] Xiao X S, Xie Y and Hao L M 2025 *Micro Nanostruct.* **205** 208191

[40] Li J Q, Xie Y and Chen Y 2026 *Micro Nanostruct.* **211** 208543

[41] Hanifan B, Jalil A and Ilyas S Z 2024 *Mater. Adv*. **5** 4366

[42] Zhao K, He D and Fu S 2022 *Nanomaterials* **12** 3418

[43] Nguyen C V and Hieu N N 2016 *Chem. Phys*. **468** 9

[44] Jia Y, Zhang Y and Wei X 2020 *J. Alloys Compd*. **832** 154965

[45] Vi V T T, Hieu N N and Hoi B D 2020 *Superlattices Microstruct*. **140** 106435

[46] Xie B, Wu J and Mei J 2024 *Nano Lett*. **24** 2870

[47] Li H, Li J and Liu F 2024 *Next Mater*. **4** 100116

[48] Zhao J, Hu Y and Xie Y 2020 *Phys. Rev. Appl.* **14** 064003

[49] Ganichev S D, Ketterl H and Prettl W 2000 *Appl. Phys. Lett*. **77** 3146

[50] Wang Y, Cui Z and Zhang C 2024 *Mater. Today Commun.* **40** 109857

[51] Cui Z, Gao X and Zhang S 2024 *Chin. J. Phys*. **91** 421

[52] Hao J, Wu J and Wang D 2023 *Phys. Status Solidi A* **220** 2200686

[53] Fu X, Lin J and Cheng X 2023 *Mater. Today Commun.* **35** 106175